

Flagellar dynamics of a connected chain of active, polar, Brownian particles

Raghunath Chelakkot, Arvind Gopinath, L. Mahadevan and Michael F. Hagan

J. R. Soc. Interface 2014 **11**, 20130884, published 18 December 2013

Supplementary data

["Data Supplement"](#)

<http://rsif.royalsocietypublishing.org/content/suppl/2013/12/17/rsif.2013.0884.DC1.html>

References

[This article cites 30 articles, 4 of which can be accessed free](#)

<http://rsif.royalsocietypublishing.org/content/11/92/20130884.full.html#ref-list-1>

Email alerting service

Receive free email alerts when new articles cite this article - sign up in the box at the top right-hand corner of the article or click [here](#)



Research

Cite this article: Chelakkot R, Gopinath A, Mahadevan L, Hagan MF. 2014 Flagellar dynamics of a connected chain of active, polar, Brownian particles. *J. R. Soc. Interface* **11**: 20130884.
<http://dx.doi.org/10.1098/rsif.2013.0884>

Received: 27 September 2013

Accepted: 27 November 2013

Subject Areas:

biomimetics, biomechanics, biophysics

Keywords:

synthetic flagella, active filament, follower forces

Authors for correspondence:

L. Mahadevan

e-mail: lm@seas.harvard.edu

Michael F. Hagan

e-mail: hagan@brandeis.edu

[†]These authors contributed equally to this study.

Electronic supplementary material is available at <http://dx.doi.org/10.1098/rsif.2013.0884> or via <http://rsif.royalsocietypublishing.org>.

Flagellar dynamics of a connected chain of active, polar, Brownian particles

Raghunath Chelakkot^{1,3,†}, Arvind Gopinath^{1,2,†}, L. Mahadevan^{3,4} and Michael F. Hagan¹

¹Martin Fisher School of Physics, Brandeis University, Waltham, MA 02453, USA

²Max Planck Institute for Dynamics and Self-Organization, Goettingen 037077, Germany

³School of Engineering and Applied Sciences and ⁴Department of Physics, Harvard University, Cambridge, MA 02138, USA

We show that active, self-propelled particles that are connected together to form a single chain that is anchored at one end can produce the graceful beating motions of flagella. Changing the boundary condition from a clamp to a pivot at the anchor leads to steadily rotating tight coils. Strong noise in the system disrupts the regularity of the oscillations. We use a combination of detailed numerical simulations, mean-field scaling analysis and first passage time theory to characterize the phase diagram as a function of the filament length, passive elasticity, propulsion force and noise. Our study suggests minimal experimental tests for the onset of oscillations in an active polar chain.

1. Introduction

Eukaryotic cilia and flagella are whip-like, elastic microstructures that undergo oscillatory beating to drive processes such as locomotion [1], mucus clearance [2], embryogenesis [3] and directed cell migration [4]. While the molecular mechanisms that control ciliary beating remain incompletely understood, it is well established that sliding forces generated by dynein motors attached to the microtubule-based backbone of cilia play a crucial role [5]. Indeed, recent experiments on a reconstituted minimal motor-microtubule system by [6] demonstrate cilia-like beating suggesting that the interplay of elasticity and activity drives the oscillations.

In addition to understanding how these active structures work in nature, there is growing interest in designing artificial analogues. Artificial beating systems driven by external periodically varying electromagnetic fields have been synthesized [7], and theoretical calculations have suggested that swimmers can be constructed from gels that undergo time-dependent swelling/de-swelling transitions in response to an external forcing periodic stimulus [8] or an internal oscillatory chemical reaction [9]. However, developing internally driven structures capable of sustained beating patterns with controllable frequencies remains a subject of intense exploration.

In this study, we use simulations and theory to identify a different mechanism, involving no oscillating external fields or concentrations, that results in controllable, internally driven flagella-like beating or steady rotation. We consider microstructures comprised of tightly connected, polar, self-propelled units, which are geometrically constrained at one end by a clamp or a frictionless pivot. The tangentially directed compression forces arising from the self-propulsion cause a buckling instability, yielding periodic shapes and motions. The mechanism we study thus corresponds to the active analogue of the continuous buckling of a filament owing to *follower forces*, which refer to compressive forces that always act along the local instantaneous tangent to the filament, and thus ‘follow’ the filament as it moves in the ambient viscous medium.

The two-dimensional chain of connected, self-propelled particles that we envision may be realized in several experimental systems. First, Janus beads can propel themselves through self-diffusophoretic [10–12] or thermophoretic effects [13,14], whereas asymmetric granular discs or rods undergo directed motion on shake tables [15–17]. These individual propelled particles can be connected to form active filaments, either through face–face attractions or by passive tethers. A second route to obtain such active polar filaments is by using motility assays in which microtubule or actin filaments are propelled by surface-grafted molecular motors, with one end of the filament constrained by pinning to the surface or through optical trapping.

In the quasi-two-dimensional aqueous settings that we consider, the surface acts as a sink of momentum that cuts off long-range hydrodynamic interactions, allowing filament elasticity and active forces to control filament dynamics. Therefore, we do not include long-range hydrodynamic interactions in our model. Our findings are thus complementary to an independent study [18,19] conducted at the same time as ours, which uses non-local Stokesian hydrodynamics to examine a filament made active by a permanent distribution of stresslets along its contour and finds that induced secondary flows can generate autonomous filament motion. Although follower forces were first proposed by Euler [20–22] they have been rarely studied in the context of active filaments moving in a viscous medium. An exception to this is the elegant linear stability analysis by Sekimoto *et al.* [23] of elastic filaments animated by molecular motor proteins. They showed that, in the noise-free limit where fluctuations in the direction of the active forces on the filament can be neglected, oscillatory behaviour arises above a critical value of the active force. Here, we combine particle-based simulations, scaling analysis and first passage time calculations to determine the large-amplitude motions of an active filament as a function of the filament length, passive elasticity, propulsion force and the magnitude of fluctuations in propulsion directions. We find that linear analysis [23] is valid for short filaments in the zero-noise limit close to criticality. However, the nonlinear response leads to different scaling relations and meandering waves that resemble motions of long flagella [24] for long filaments or for strong active force densities. Importantly, we also combine extensive simulations and theory to identify the ability of noise to disrupt the emergent oscillations in these systems.

In §2, we describe the model, the computational implementation and the dimensionless parameters that govern system behaviour. Section 3.1 describes our dynamical simulation results in the limit of weak noise for anchored short filaments. We also present mean-field scaling arguments that enable us to obtain explicit expressions for the critical force f_c required to obtain oscillatory states as well as the frequency and wavelength of oscillations. In §3.2, we analyse the dynamics for very long filaments, or filaments that are subject to very high compressive force densities. We find that excluded volume interactions and the avoidance of self-contact results in looped shapes as well as a change in the frequency–activity relationship. We then explore the effect of noise in §3.3, where we identify the transition from steady, correlated oscillations to erratic, uncorrelated oscillations. A first passage time calculation based on transition state theory allows us to identify the critical noise level required to destabilize steady oscillations. We conclude in

§4 by situating our work in the context of current research on active motile filaments.

2. Model

Our model for the active filament is a two-dimensional chain of connected, self-propelled, polar colloidal spheres. The chain (filament) has N such spheres each of diameter σ located at coordinates \mathbf{r}_i ($i = 1, \dots, N$) interacting via harmonic potential with the equilibrium linker length being b , so that

$$U_l = \frac{\kappa_l}{2k_B T} \sum_{i=1}^{N-1} (|\mathbf{r}_{i+1} - \mathbf{r}_i| - b)^2.$$

The value of κ_l is maintained at a value large enough that the actual distance between each polar particle is nearly b , making the chain nearly inextensible. Additionally, resistance to chain bending is implemented via a three-body-bending potential

$$U_b = \frac{\kappa}{2k_B T} \sum_{i=2}^{N-1} (\mathbf{b}_{i+1} - \mathbf{b}_i)^2,$$

where $\mathbf{b}_i = (\mathbf{r}_i - \mathbf{r}_{i-1})/|\mathbf{r}_i - \mathbf{r}_{i-1}|$ is the unit bond vector that is anti-parallel to the local tangent and κ is the bending rigidity. The whole system moves in a fluid of viscosity μ , and the system is held at constant temperature T .

To enable active compressive forces to act on neighbouring spheres, we bias them to preferentially align with the instantaneous tangent vector. This is consistent with the interaction between a motor head and a filament in a motility assay, where attached motors walk and exert forces along the filament track, or self-propelled Janus spheres connected by face–face attractions, where the propulsion direction is normal to a face. The polar direction $\hat{\mathbf{p}}_i$ for each sphere is biased to point along \mathbf{b}_i by a harmonic potential

$$U_a = \frac{\kappa_a}{2k_B T} (\hat{\mathbf{p}}_i - \mathbf{b}_i)^2, \quad (2.1)$$

with κ_a controlling the magnitude of polarity fluctuations about the mean direction.

In the limit $\kappa_a \rightarrow \infty$, the propulsion forces are perfectly aligned with the local tangent (the idealized follower-force scenario). This limit corresponds to an experimental system in which the chemical linkage between successive beads in the filament is tightly coupled to and parallel to the direction of the self-propulsion. Lower values of κ_a represent reduced coupling and thus result in a fluctuating polarity. This situation could arise either from thermal noise or from additional interactions, e.g. in the case of a microtubule–motor system, lateral interactions between the motor head and its neighbours could result in fluctuating polarity.

The dynamics of the filament is determined by the evolution of the sphere positions \mathbf{r}_i and orientations $\hat{\mathbf{p}}_i$, ($i = 1, \dots, N$) which we simulate using over-damped Brownian dynamics,

$$\left. \begin{aligned} \dot{\mathbf{r}}_i &= \frac{1}{k_B T} D (\mathbf{F}_i^l + \mathbf{F}_i^b + \mathbf{F}_i^{\text{Ex}}) + \frac{1}{k_B T} D f_p \hat{\mathbf{p}} + \sqrt{2D} \zeta_i \\ \dot{\hat{\mathbf{p}}}_i &= \frac{1}{k_B T} D \tau_i \times \hat{\mathbf{p}}_i + \sqrt{2D} \tau_i^{\text{r}} \end{aligned} \right\} \quad (2.2)$$

Here, $\mathbf{F}_i^l = -\partial U_l / \partial \mathbf{r}_i$, $\mathbf{F}_i^b = -\partial U_b / \partial \mathbf{r}_i$ and $f_p \hat{\mathbf{p}}$ are respectively the axial, bending and propulsion forces, $\tau_i = -\hat{\mathbf{p}}_i \times \partial U_a / \partial \hat{\mathbf{p}}_i$ is the torque arising from the angular potential,

$\mathbf{F}_i^{\text{Ex}} = -\partial U_{\text{ex}}/\partial \mathbf{r}_i$ is a pairwise excluded-volume repulsive force given by the Weeks–Chandler–Andersen (WCA) potential

$$U_{\text{ex}}(r_{ij}) = 4\epsilon \left[\left(\frac{\sigma}{r_{ij}} \right)^{12} - \left(\frac{\sigma}{r_{ij}} \right)^6 \right] + \epsilon \quad \text{if } r_{ij} < 2^{1/6},$$

and zero otherwise [25]. This pairwise interaction applies to all pairs of beads in close spatial proximity, including both nearest neighbours along the chain and those which are non-local in sequence. The translational and rotational diffusion constants D and D_r in our over-damped system satisfy the Stokes–Einstein relationship $D_r = 3D/\sigma^2$, and ζ and ζ^r are zero mean, unit variance Gaussian white noise forces and torques respectively, with covariances that satisfy

$$\left. \begin{aligned} \langle \zeta_i(t) \zeta_j(t') \rangle &= 2\delta(t-t') \delta_{ij} \delta \\ \langle \zeta_i^r(t) \zeta_j^r(t') \rangle &= 2\delta(t-t') \delta_{ij} (\delta - \hat{\mathbf{p}}\hat{\mathbf{p}}) \end{aligned} \right\} \quad (2.3)$$

As the viscous mobility of a sphere is isotropic, our simulations neglect differences in viscous resistance to normal and tangential modes of filament motion. We do not include hydrodynamic interactions between parts of the filament in our model; these can be neglected in the quasi-two-dimensional dense viscous systems we are motivated by due to screening resulting from confinement. In the limit of a single sphere, our model reduces to the over-damped description of a self-propelled particle, which undergoes a persistent random walk with mean instantaneous speed $v_p = f_p D/k_B T$, persistence length v_p/D_r and an effective diffusion coefficient $D_{\text{eff}} \sim D + v_p^2/D_r$.

We define the arc-length parameter s in the range $0 \leq s \leq \ell \equiv Nb$ to parametrize the coarse-grained position along the filament. Finally, we make the equations dimensionless by using σ and $k_B T$ as basic units of length and energy, and σ^2/D as the unit of time and we set $\epsilon = k_B T$.

Simulations were initialized using a straight configuration with the filament vertically oriented along $\hat{\mathbf{e}}_x$, with all \mathbf{p}_i initially along $-\hat{\mathbf{e}}_x$. One end of the filament corresponding to $s = \ell$ was always free. The anchored end $s = 0$ was either clamped vertically or attached to a frictionless pivot with the filament free to rotate. The clamping was achieved by attaching the first particle at ($s = 0$) to a fixed point in space \mathbf{r}_0 by a harmonic potential with the same properties as the binding potentials between the other particles in the filament. While the three-body-bending potential applied on \mathbf{r}_1 has an equilibrium angle of $\pi/2$ between the bond vector $\mathbf{r}_1 - \mathbf{r}_0$ and $\hat{\mathbf{e}}_y$.

3. Results

To investigate the dependence of filament behaviour on the system parameters, we performed simulations with filaments anchored according to clamped or pivoted boundary conditions for varying filament length ℓ , active force density f_p and angular stiffness. The angular stiffness parameter, κ_a , was varied from 0.1 to 20, to investigate situations from the noise-free idealized follower-force limit ($\kappa_a \rightarrow \infty$) to the noise-dominated regime. For all simulations described here, we set the bending rigidity $\kappa = 2 \times 10^4$ to give a persistence length $L_p \gg \ell$.

The images in figure 1 illustrate our main results. First, we find that for a given filament length, the straight filament configuration becomes unstable above a threshold propulsion force, and the system displays an oscillatory motion. The boundary condition at the anchored end dramatically

changes the mode of oscillation. A clamped end results in flagella-like beating, whereas a pivoted end allows the filament to rotate freely, forming spiral shapes. Second, in the low noise limit, we observe a second critical length beyond which the beating and rotating shapes start to depend critically on the excluded volume interactions. Finally, above a threshold noise level, the system transitions from periodic oscillations to erratic motions. Thus, the noise-level provides an independent, experimentally accessible parameter with which to tune the filament behaviour.

For the sake of simplicity, the simulations presented in the main text assumed local resistivity theory for the hydrodynamics and isotropic filament mobility. However, we have tested these approximations by performing additional simulations with (i) an anisotropic mobility (corresponding to a true slender body) and, (ii) non-local hydrodynamic interactions implemented using a coarse-grained fluid model called multiparticle collision dynamics [26] (see appendix C for details and results). While relaxing these approximations leads to quantitative differences in beating frequencies and the trajectories of filament material points, the dynamical behaviours and phase properties of the system remain qualitatively the same.

3.1. Dynamics for short filaments and weak activity

We first present results for the case of a clamped filament, with boundary conditions at the anchored end given by $\mathbf{b}_0 = \hat{\mathbf{e}}_x$, and $\mathbf{r}_0 = 0$. The other end is force- and torque-free. For weak noise ($\kappa_a \gg 1$), fluctuations in polarity along the filament are negligible, and the base state is a straight filament. The internal active forces act along the filament towards the clamped end, leading to compression. When the internal propulsion force f_p exceeds a critical value f_c , which depends on ℓ and κ_a , the filament buckles, in a manner similar to a self-loaded elastic filament subject to gravity. However, the post-buckled states are quite different (see electronic supplementary material, appendix A), because the direction of active force density follows the polarity vectors $\hat{\mathbf{p}}_i$ and thus tends to point along the filament axis.

At fixed filament stiffness κ , and for $f_p > f_c$, we find that the magnitude of the polarization stiffness κ_a controls the long-time dynamics of the filament. In figure 2a, we show the local filament curvature as a function of time and arc length. For small values of κ_a (left), thermal diffusion controls the local orientation of $\hat{\mathbf{p}}_i$, and the propulsion activity is uncorrelated along the filament. In this regime, the filament dynamics is marked by transients resulting from the bending generated by the particle propulsion, but no coherent patterns. When κ_a is increased above a critical value κ_a^c , the polarities of the spheres align strongly with the local tangent. The resultant self-propulsion force is strongly correlated with the filament tangent and the filament oscillates with periodic, large-amplitude wavy motions (the plot on the right) that propagate from the proximal (clamped) end to the distal (free) end. This beating profile is very similar to that of flagella in eukaryotic cells, though the underlying physics differs fundamentally.

We quantify the regularity of oscillations by measuring the length of the end–end vector $L_{\text{ee}} = \sqrt{(\mathbf{r}_N - \mathbf{r}_1) \cdot (\mathbf{r}_N - \mathbf{r}_1)}$, as a function of time, shown for two values of κ_a , $\kappa_a < \kappa_a^c$ and $\kappa_a \gg \kappa_a^c$, in figure 2b. While L_{ee} displays large variations in time for both values of κ_a because of the large propulsion

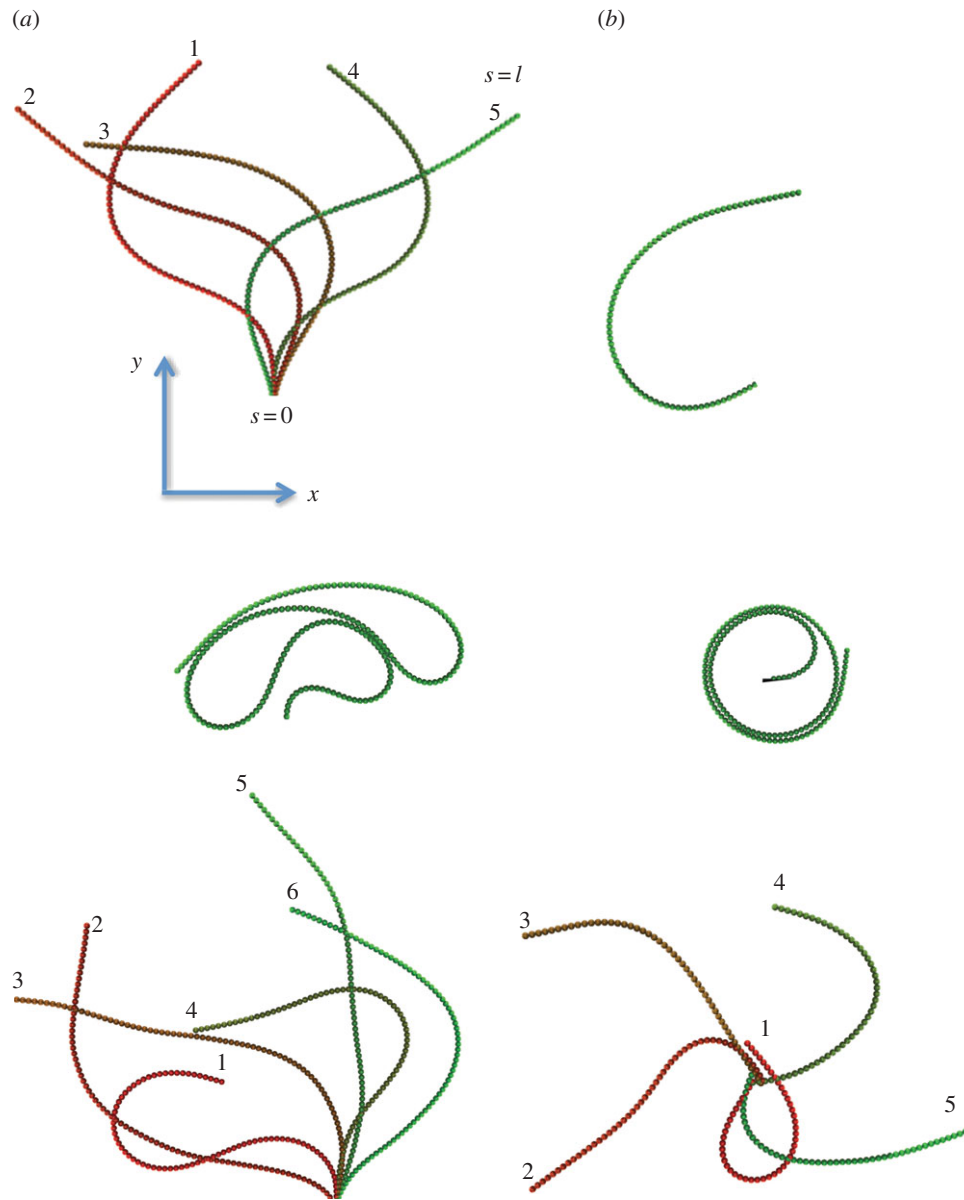


Figure 1. Overview of the dynamical shapes observed in simulations. The active force density is f_p , filament length is ℓ and the angular noise is parametrized by κ_a . (a) Shapes for a filament clamped at one end. (Top) Regular beating for short filaments, $\ell = 80$ with weak angular noise $\kappa_a = 20$. The frequency of oscillations is controlled by f_p . (Centre) Self-contacting looped shapes observed for long filaments $\ell = 160$ with weak noise $\kappa_a = 20$. Excluded-volume interactions alter the frequencies of oscillating and rotating shapes in this limit. (Bottom) For large angular noise, $\kappa_a = 0.5$, motions along the filament decorrelate, resulting in highly erratic shapes. (b) Spiral shapes for a filament with one free end and one end that can pivot. (Top) A weakly curved filament of $\ell = 50$ rotating at constant frequency, typical of short filaments and weak noise $\kappa_a = 20$. (Centre) A rotating, tightly wound spiral typical of long filaments $\ell = 160$ and weak noise $\kappa_a = 20$. (Bottom) Erratic rotation without a steady rotating shape or well-defined rotational frequency, typical of strong noise, $\kappa_a = 0.5$ for a filament with $\ell = 80$. In all cases shown the active force density was $f_p = 20$. The value of bending stiffness is $\kappa = 2 \times 10^4$ in all figures in the article. Animations from typical simulations are provided in the electronic supplementary material. (Online version in colour.)

force, the profile for $\kappa_a \gg \kappa_a^c$ is periodic, and its power spectral density shows a distinct frequency maximum (figure 2c).

To understand our numerical experiments and to obtain estimates for the critical buckling load and the frequency of ensuing oscillations in the periodic regime, we consider the noiseless limit $\kappa_a \rightarrow \infty$, and coarse-grain the chain of spheres into a slender, elastic filament of length ℓ and bending stiffness κ . The force owing to the self-propulsion translates to a compressive force per unit length of strength f_p oriented anti-parallel to the local tangent vector. The resulting internal propulsion force $f_p \ell$ deflects the tip by a small transverse distance $h \ll \ell$ leading to an effective filament curvature $O(h/\ell^2)$. Balancing moments about the base then yields

$hf_p \ell \sim \kappa h/\ell^2$ and thence the critical propulsion force beyond which the straight filament is no longer stable,

$$f_c \sim C_1 \left(\frac{\kappa}{\ell^3} \right). \quad (3.1)$$

The constant C_1 is, in principle, a function of κ_a (note that $\kappa_a \gg 1$ still holds) and thus must be determined from simulations close to the critical point. For the particular case $\kappa_a = 100$, we find that $C_1 \approx 78$ (figure 3a). Thus a chain immersed in a viscous fluid cannot sustain a static buckled state and instead yields to oscillating, deformed shapes (see electronic supplementary material, appendix A).

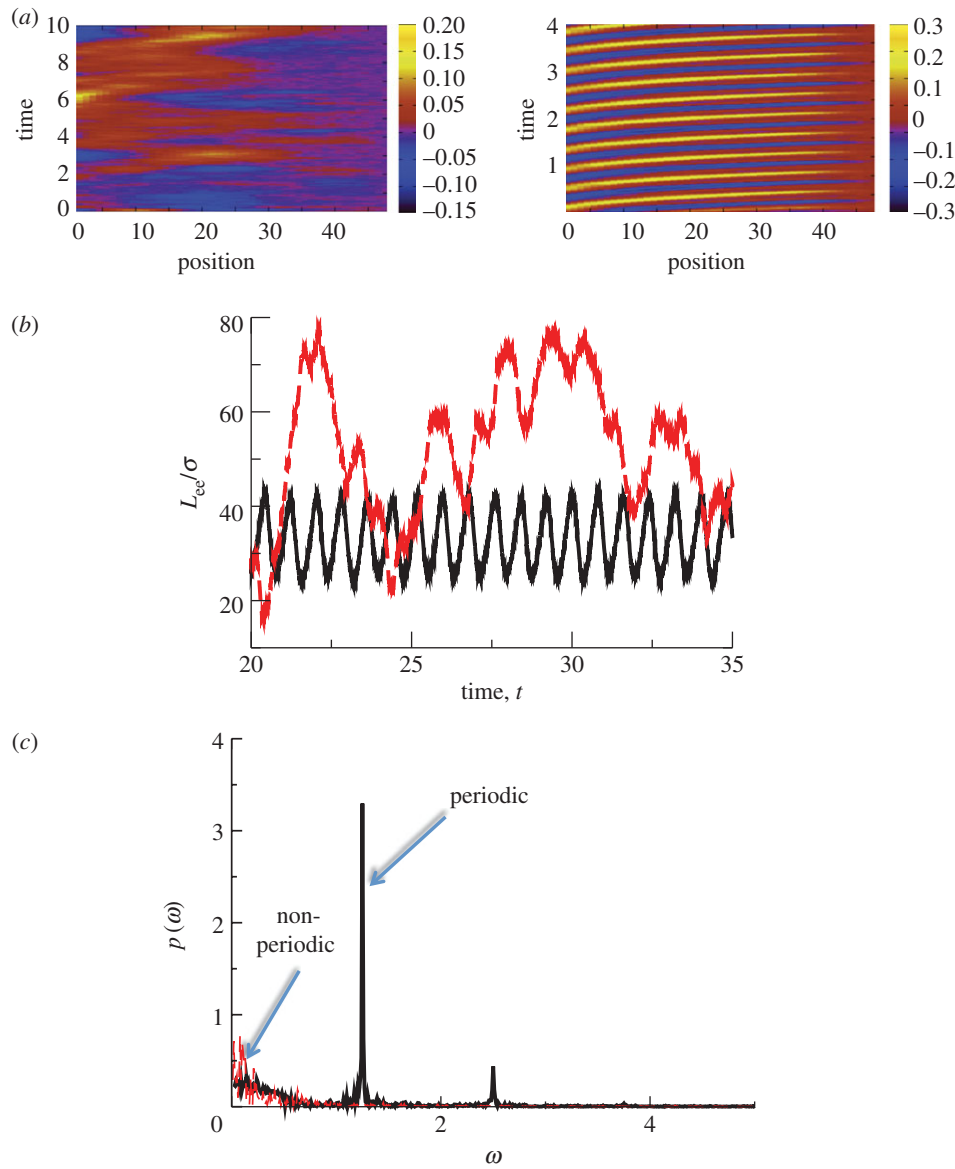


Figure 2. (a) Plots of the local filament curvature as a function of time and the distance from the clamped end for a filament of length $\ell = 80$ and active force density $f_p = 20$, for typical examples of non-periodic beating for angular force constant $\kappa_a = 0.5$ (left) and periodic buckling for angular force constant $\kappa_a = 20$ (right). (b) Length of the end–end vector L_{ee} as a function of time for periodic buckling (solid line) and non-periodic beating (dashed line). (c) Power spectral density of L_{ee} for filament length $\ell = 80$, propulsion force $f_p = 20$, and angular force constant $\kappa_a = 20$ (periodic) and $\kappa_a = 0.5$ (non-periodic). (Online version in colour.)

In the noise free limit, the constant C_1 ($\kappa_a \rightarrow \infty$) can be exactly obtained from a stability analysis of the corresponding continuum mean-field equations. A systematic derivation of the full nonlinear equations governing the filament dynamics that builds on a local resistivity formulation relating filament bending to its velocity yields two coupled nonlinear equations for the tension in the filament T and θ , the angle the filament makes with e_x (see electronic supplementary material, appendix B). In this linear limit, the single dimensionless parameter that determines the existence and emergence of solutions is indeed the dimensionless number $(f_p \ell^3 / \kappa)$. The linearized equations corresponding to the noise-free, mean-field version of model were considered earlier [23]. The critical value of the dimensionless parameter at onset of oscillations was determined to be 75.5, which closely matches the numerical value we obtain for $\kappa_a = 100$.

When $(f_p - f_c)/f_c \gg 1$ and the straight filament is unstable, the characteristic length over which the active

compression is accommodated

$$\lambda \sim C_2 \left(\frac{\kappa}{f_p} \right)^{1/3}, \quad (3.2)$$

is given by $\lambda \ll \ell$. In the over-damped limit, all the energy supplied by the self-propulsion transforms first into elastic bending energy and is then dissipated viscously by the filament motion. In a time ω^{-1} , the energy dissipated viscously is the product of the force per unit length $\eta_\perp \lambda \omega$, the characteristic deflection λ and the velocity $\omega \lambda$. This dissipation has to balance the active energy input into the system owing to the self-propulsion $f_p \lambda^2 \omega$, yielding $\eta_\perp \lambda^3 \omega^2 \sim f_p \lambda^2 \omega$. Using equation (3.2), we obtain the oscillation frequency

$$\omega \sim C_3 \left[\frac{1}{\eta_\perp} \left(\frac{f_p^4}{\kappa} \right)^{1/3} \right], \quad (3.3)$$

which shows excellent agreement with our simulations for a range of active forces at constant ℓ . Simulations performed

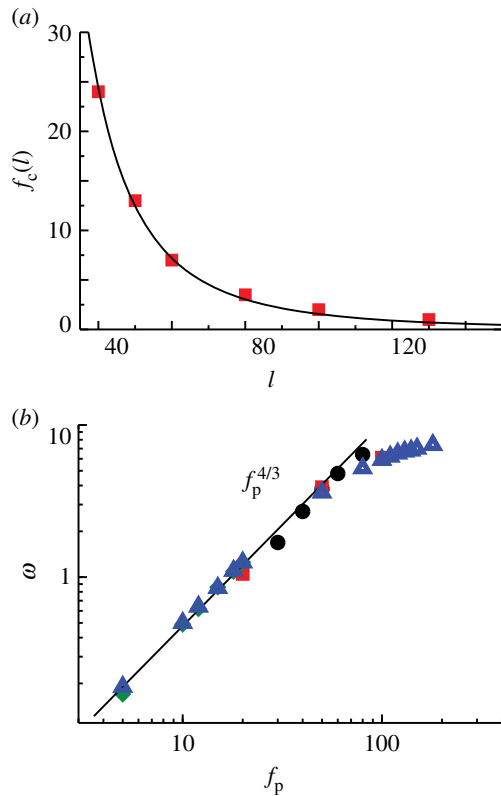


Figure 3. (a) Critical propulsion force $f_c(\ell)$ for various filament lengths, at constant angular stiffness $\kappa_a = 100$. The solid line is $f_c = C/\ell^3$ with $C \simeq 78$, consistent with the theory (equation (3.1)). (b) The beating frequency of filaments as a function of propulsion force f_p for filament lengths $\ell = 40$ (filled circles), $\ell = 50$ (filled squares), $\ell = 80$ (filled diamonds), and $\ell = 100$ (filled triangles). The dashed line corresponds to the scaling law (equation (3.3)). Parameters are dimensionless as described in the text. For very long lengths, the filament becomes self-interacting resulting in a decrease in the exponent due to excluded-volume interactions. (Online version in colour.)

with anisotropic filament mobility with $\eta_{\perp} = 2\eta_{\parallel}$ instead of $\eta_{\perp} = \eta_{\parallel}$ yield qualitatively similar results (see electronic supplementary material, appendix C). However, comparing with the filament with isotropic mobility, the beating frequency is reduced roughly by half as predicted by equation (3.3) obtained from scaling arguments. For very high values of f_p (or equivalently for long filaments), we find that the frequency obeys a different scaling law, for reasons discussed in the next section.

The beating motions described above require a clamped boundary condition that prevents both rotation and translation. We next performed simulations for a filament moving about a frictionless, pivoting end at $s = 0$ such that $r_0 = 0$ but b_0 is unconstrained.

For small values of κ_a , and with the contour length ℓ and rigidity κ held fixed, the filament end–end length L_{ee} displays large irregular variations and the end–end vector L_{ee} undergoes irregular rotation about the fixed end—illustrated in figure 1c. Increasing the value of κ_a results in the active forces being increasingly correlated along the contour. The post-buckled filament now assumes that a steadily rotating bent shape and the value of L_{ee} does not vary in time (figure 1b).

The rotation frequency extracted from simulations by calculating the orientation of L_{ee} as a function of time is plotted in figure 4 as a function of f_p . When $\ell \ll (\kappa/f_p)^{1/3}$, the

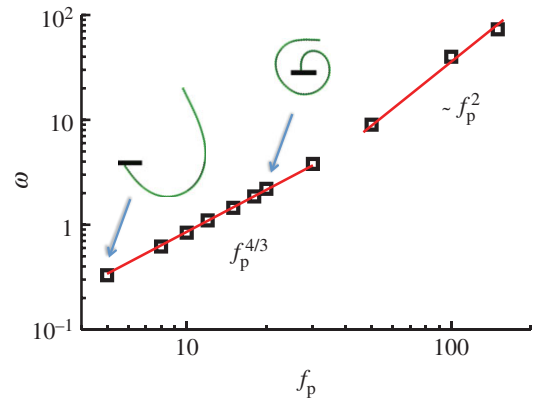


Figure 4. Frequency of steady rotation for a filament anchored at a pivot, with length $\ell = 160$, angular force constant $\kappa_a = 2 \times 10^2$, and bending stiffness $\kappa_b = 2 \times 10^4$. The snapshots illustrate typical shapes of the rotating filaments. For weak forcing, the filament is lightly coiled. As the force density increases, the filament starts to curve significantly almost closing in on itself. Finally for strong forcing (or equivalently for long filaments), the final stable rotating shapes are highly nonlinear, tightly wound coils and the frequency scaling deviates from the $4/3$ power law. (Online version in colour.)

filaments are short compared with the characteristic wavelength and do not overlap. Non-local interactions between segments of the filament can then be neglected and the steady rotational frequency varies with force in accord with equation (3.3). The shapes we obtain compare well with the experimental observed conformations in motility assays where filaments animated by underlying molecular motors encounter pinning sites (defects) and start to rotate [27]. While the scaling for the critical active density above which rotation occurs follows equation (3.1), the corresponding value of the dimensionless parameter $C_1(\kappa_a)$ differs from that for the clamped case owing to the different boundary condition. For $\kappa_a = 6$, we obtain the value $C_1 \sim 36$, which compares well with the value of 30.6 obtained in the mean-field noise-free limit [23].

3.2. Self-avoidance modifies the steady frequency for strong activity or long filaments and modifies the resulting shapes

3.2.1. Clamped end

We now focus on the limit of strong activity $f_p \gg (\kappa/\ell^3)^{1/3}$ or long filaments $\ell/\lambda \gg 1$ for which large filament curvatures cause non-local segments to interact. For a clamped filament, these non-local interactions result in loopy curves with highly curved regions interspersed by relatively flat ones as shown in figure 1b.

In figure 5, we compare the filament trajectories exhibited by non-interacting filaments with the self-interacting filaments. The length is held constant for the case illustrated, whereas the active force density is tuned to different values. For non-interacting filaments, material points on the filament execute closed trajectories resembling a figure-of-eight, as expected for an inextensible, non-interacting, oscillating filament. Points near the free end undergo larger deformations and thus larger amplitude oscillations when compared with points near the base. Increasing the force density to $f_p = 50$ yields dramatically different behaviours. First, the free end of

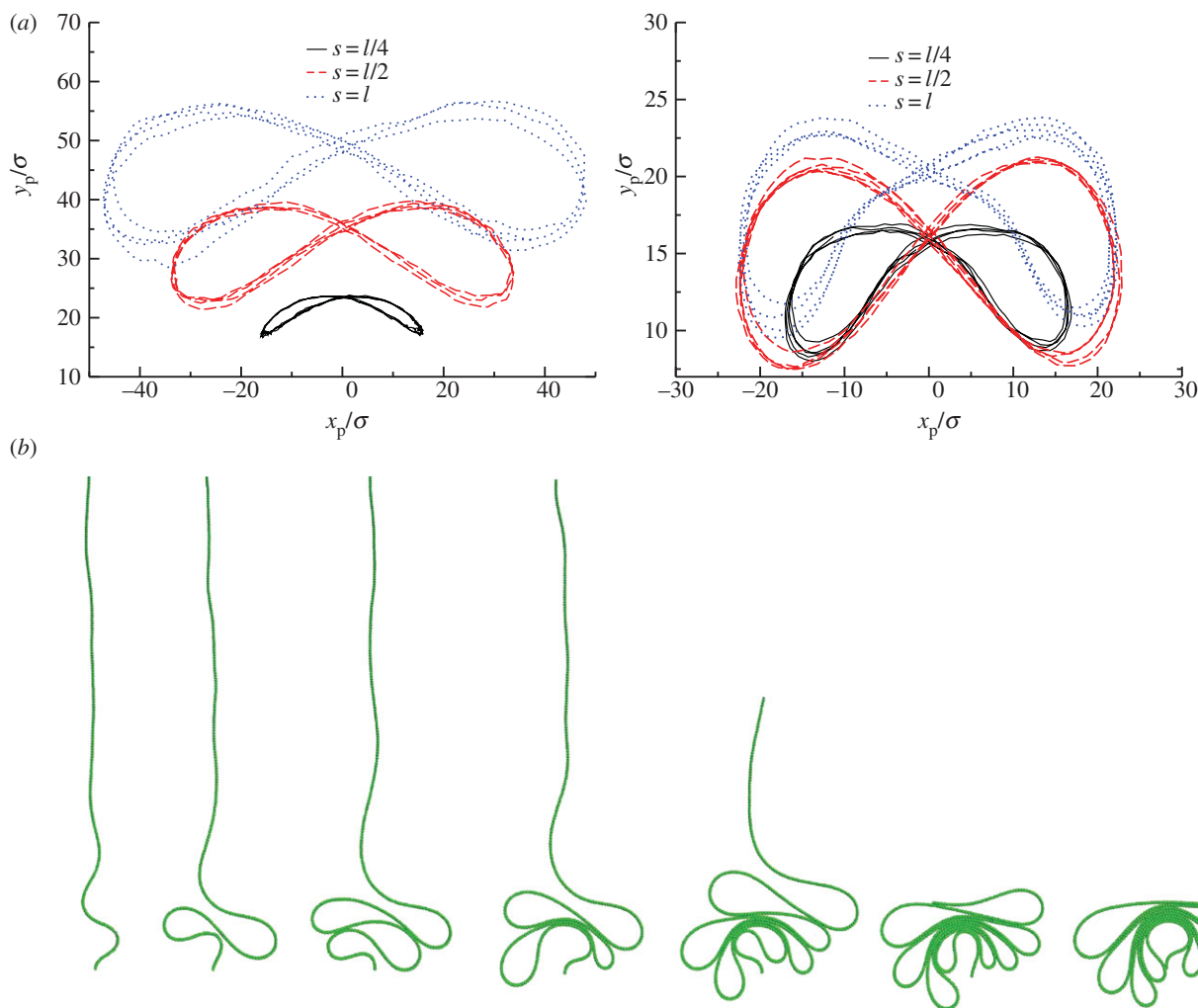


Figure 5. Comparison between clamped filaments in the non-self-interacting case (small ℓ or small f_p) and the self-interacting case (large ℓ or large f_p). Trajectories of material points are shown for $\ell = 100$ and varying force density f_p . (a) Left: results for $f_p = 5$ (non-interacting). The strength of the compressive forces are low enough that there is no interaction between segments separated along the filament contour by more than a few σ . (a) Right: a larger force density $f_p = 50$ (self-interacting) yields more curved and loopy structures. Note the dramatic change in the difference between trajectories for $s = \ell$ and $s = \ell/4$. (b) A sequence of snapshots from a simulation in which an initially straight long filament buckles into a series of successively meandering loops. As time increases (moving right), we find that self-avoidance and bending control the number and lateral extent of the loops. Loops formed initially are trapped by those that form later. Eventually, most of the filament moves tangentially resulting in large parts of the filament undergoing lateral sliding. The first three snapshots from the left do not show the full length of the filament. (Online version in colour.)

the filament extends a greater distance in the vertical, downward direction owing to larger buckling. More importantly, trajectories exhibit significant self-interaction (compare, for instance, the locus of $s = \ell$ and $s = \ell/4$ in the two cases) and oscillate with smaller frequencies. The frequency–activity response is characterized by a power law exponent different from that obtained for non-interacting filaments (equation (3.3)). This modification may arise due to additional energy dissipation resulting from excluded-volume interactions as two filaments slide past each other in close proximity. We also note that in a setting where hydrodynamic interactions are not screened, the frequency will be modified by anisotropic drag effects and direct fluid-mediated interactions between non-local parts of the filament (see electronic supplementary material, appendix C).

Interestingly, the looped conformations we observe in the self-interacting case resemble the meandering waveforms seen in studies of quail spermatozoa [24], which have unusually long flagella. Meandering waveforms are also observed in a very viscous fluid or close to boundaries that resulted in

increased local viscous resistivity such as near a coverslip. While the waveforms observed in experiments were almost static in relation to the field of view with bend propagation manifested as the forward movement of the flagellum through the static shape, in our simulations, because one end of the filament is clamped no such steady motion is possible. Thus, the loops that form first are continuously trapped by loops that form subsequently (figure 5b). An initially straight filament culminates in a tangle of continuously sliding looped structures with most of the filament moving tangentially.

3.2.2. Pivoted end

Changing the boundary condition at one end to a pivot yields tightly coiled, rotating structures as shown in figure 1b and figure 6b. At steady state, the final radius, R_c , decreases sharply with f_p ; eventually bending of the coil is balanced by the lateral forces owing to excluded volume, resulting in a very slow decay with f_p . In figure 6a, we plot the radius of the coiled

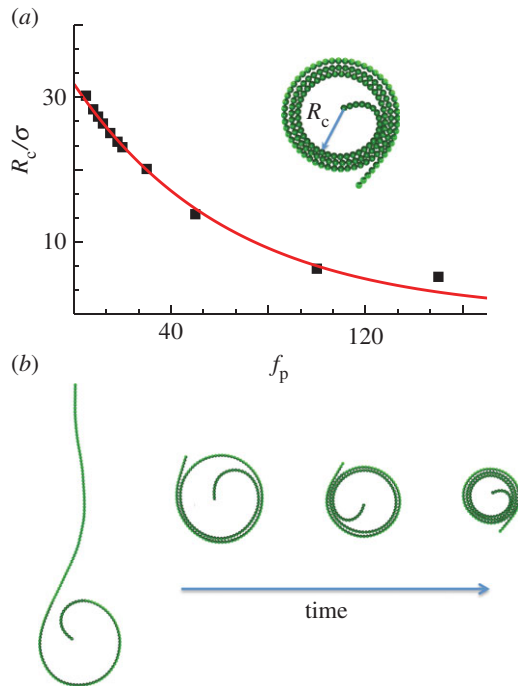


Figure 6. Radius R_c of the final coiled shape as a function of f_p for a filament with a pivoting end. The parameter values are $\ell = 160$, $\kappa_a = 2 \times 10^2$ and $\kappa = 2 \times 10^4$. The solid curve indicates a fit to an exponential decay. (b) Transient shapes for very large f_p as the filament coils and eventually undergoes steady rotation. (Online version in colour.)

shapes and find an initial exponential decay with the active force f_p (red curve).

Snapshots of the transient rotating shapes seen for long filaments (figure 3b) indicate multiple timescales in the coiling process. Initially, the filament curvature increases with a characteristic rate, until the free end closely approaches another region of the filament. Next, the remaining length is accommodated in concentric coils, whereas the curvature near the free end remains nearly constant. Once the entire filament is coiled, the curvature increases further, leading to a tightening of the coils, an increase in the number of coils, and a decrease in the coil radii. The filament behaves nearly as a rigid body, with negligible sliding between adjacent coils. The frequency of steady rotation depends strongly on excluded volume forces. For fixed ℓ , the frequency almost scales as f_p^2 (see figure 4 in the large f_p limit). When the same simulations were rerun without excluded-volume interactions, we obtained completely overlapping coils and a frequency that scaled as $f_p^{4/3}$, consistent with equation (3.3).

4. Correlation length of polarity controls dynamics for strong noise

In previous sections, we explored the dynamics of the active polar filament in the limit of small noise (large angular stiffness κ_a), where each $\hat{\mathbf{p}}_i$ points predominately along the filament and in the direction opposite to the local tangent. We now consider the response of connected self-propelled particles as a function of κ_a and active force density f_p . Figure 7 shows the phase diagrams for (i) clamped filaments and (ii) rotating filaments.

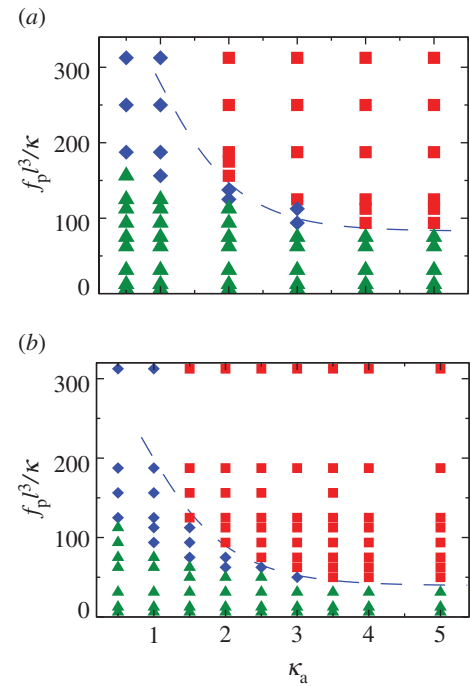


Figure 7. Phase diagram for (a) a clamped filament and (b) a rotating filament with bending stiffness $\kappa = 2 \times 10^4$. Triangles correspond to no beating, diamonds to irregular beating and squares to regular beating. The dashed curve (valid for $\kappa_a \gg 1$) corresponds to equation (4.1). The constants A (obtained from the critical value of the active force at onset for $\kappa_a \gg 1$) and B (determined by eye) are (a) $(A, B) = (78, 80)$ and (b) $(A, B) = (36, 70)$. (Online version in colour.)

As expected from the mean-field analysis in §3.1, for propulsion forces below the critical value $f_p < f_c$, we do not observe statistically significant beating (green triangles)—the straight configuration remains stable and variations in $\langle L_{ee} \rangle \simeq \ell$ owing to fluctuations of $\{\hat{\mathbf{p}}_i\}$ are insignificant. The critical value of f_c that separates this regime from the unsteady (periodic as well as non-periodic) regime is a function of the passive filament elasticity (ℓ and κ) and κ_a . In the low noise limit, f_c tends to the values estimated in §3.1 from simulations.

Keeping κ_a fixed and increasing f_p to beyond the critical value renders the straight configuration unstable and results in persistent unsteady shapes. For small values of $\kappa_a (\leq 1)$, we observe irregular beating. As κ_a is increased ($\kappa_a > 1$), the enhanced correlation of particle propulsion directions results in two trends—evident both for the clamped—shown in figure 7a—and pivoted—see figure 7b—cases. First, the critical propulsion force f_c to destabilize the straight configuration decreases, saturating to the continuum limit as $\kappa \rightarrow \infty$. Second, the beating becomes periodic. Interestingly however, for any $\kappa_a \gtrsim 1$, there persists a diminishing region of irregular beating between the stationary and periodic-beating regions. This region of irregular (or erratic) beating is characterized by variations in shape and the rates at which local curvatures change. As f_p increases at constant κ_a , we go from the no-beating regime (A) to an intermediate irregular beating regime (B) and finally to the regular beating regime (C). Note that the critical active force density that separates both transitions ($A \rightarrow B$ as well as $B \rightarrow C$) depends on the passive filament elasticity (ℓ and κ) and also on κ_a .

To understand the mechanisms underlying these transitions, we adopt a simplified picture of the local dynamics

and fluctuating forces generated by the self-propelled spheres. We separate $f_p(s)$ into an average part and a rapidly fluctuating part: $f_p(s) = \langle f_p(s) \rangle + \hat{f}_p(s)$. Significant fluctuations in filament conformations arise when orientations $\hat{\mathbf{p}}_i$ escape from a favourable configuration (anti-parallel to the tangent) to an unfavourable configuration where the local contribution to the active force is negligible.

When $\kappa_a \leq 1$ in the diffusion (noise)-dominated limit $\kappa_a \ll 1$, the active, polar spheres are very animated, reorienting themselves constantly on a rotary timescale $1/D_r$. As κ_a is increased from unity with the force density held fixed, the enhanced correlation of $\hat{\mathbf{p}}_i$ results in two trends. First, at some value of κ_a , the force density becomes large enough to destabilize the straight configuration resulting in a regime characterized by erratic beating. In this regime, the mean active force density is large enough to cause buckling over the entire length of the filament ℓ and the orientation potential well has a depth large enough that few polar spheres reorient. Thus, with increasing κ_a , there is both an increasing spatial correlation of $\hat{\mathbf{p}}_i$ along the filament and an increasing time over which the correlations are sustained. This irregular beating arises whenever the correlation time of propulsion directions, T_c , is shorter than the filament oscillatory timescale in the noiseless, perfectly aligned limit.

To estimate T_c , we use a first passage time calculation (see electronic supplementary material, appendix D). Treating the polarity as a continuous field $p(s)$, we define $\zeta(s)$ to be the angle between the a local polarity vector and $-t(s) \equiv b(s)$, where $t(s)$ is the tangent vector. We seek the characteristic time for a local patch of spheres to escape from a perfectly aligned configuration, in which they can drive filament compression, to a non-compressive configuration. Without loss of generality, we choose the latter to be a configuration in which the polarity vector and the local tangent are in the same direction ($\zeta = \pi$), so that the forces are extensional and thus no compressive instabilities are possible. Rewriting the angular potential (equation (2.1)) as $U_a(\zeta) = \kappa_a(1 - \cos\zeta)$, we find that the energy difference between the two configurations is $U_a(\pi) - U_a(0) = 2\kappa_a$. In the over-damped limit and for $\kappa_a > 1$, the orientations evolve diffusively, and the escape flux can be related to a frequency of crossovers or disrupting frequency. We estimate T_c using the steepest descent method [28] and ignore multiplicative factors, because our simulations are for constant diffusivities and temperature. The balance $T_c^{-1} \sim \omega$ provides a preliminary estimate for the activity separating irregular from regular beating:

$$f_p^* \sim \kappa_a^{3/4} (e^{-2\kappa_a})^{3/4}$$

This estimate however needs to be modified further. First, a non-zero critical density for buckling arises owing to the non-generic initial configuration. However, once buckled, the net force determines the beating, and the beat frequency is a function of f_p , not $(f_p - f_c)$. Thus, the critical density should tend to the continuum noise-free limit. Second, the irregular beating behaviour requires that a critical number of motors escape from the well. Satisfying these conditions leads to the dimensionless estimate

$$\left(\frac{f_p \ell^3}{\kappa} \right)^* \sim A + B \kappa_a^{3/4} (e^{-2\kappa_a})^{3/4}. \quad (4.1)$$

Here A is a constant which ensures that the result reduces to the noise-free value and is thus *not* a fitting parameter. The constant B is a measure of the critical number of motors that need to reorient to disrupt beating and we estimate it by fitting to

computational data. We interpret it as the minimal size of the patch (equivalently force) required to cause beating irregularities. While strictly valid for $\kappa_a \gg 1$, this expression—plotted as the dashed blue line in figure 7a,b—satisfactorily captures the shape of the boundary for $\kappa_a > 1$.

5. Conclusion and outlook

Our study suggests a simple proposal to mimic the beating of eukaryotic flagella. Rather than having motors that walk on adjacent filaments that are clamped at an end, we have shown that we can generate actively oscillating and rotating filaments using connected self-propelled particles. The frequency of oscillations and thereby the swimming speed and fluid forces can be controlled by varying the dimensionless parameters in our problem—the ratio of the chain stiffness to the polarity stiffness κ/κ_a , the scaled active force $\ell^3 f_p/\kappa$, and the aspect ratio of the chain ℓ/σ , or equivalently the number of active particles. Furthermore, if the angular potential is written as $U_a = \kappa_a/2[(\hat{\mathbf{p}}_i - \mathbf{b}_i)^2 - C]$, where $0 < C \leq 1$, thus introducing a preferred direction different from the local tangent, then the initial symmetry-breaking bifurcation is eliminated and the filament will always beat. All of these parameters, in principle, are accessible experimentally. In particular, recent efforts to manipulate connected passive colloids by electrical fields [29], microfluidics [30], lock-and-key type interactions [31] and heat [29] have been quite successful in yielding externally actuated filaments with controllable bending stiffness. Extension of such techniques using diffusophoretic Janus particles as templates should yield internally controlled self-propelling filaments, just as a small variation of the motility assay for rotating filaments [27], by clamping an end, will lead to beating. However, the quantitative experiments to check our predictions remain to be done.

The relationship between noise and beating patterns, a key aspect of our study, is relevant in several contexts. First, our analytical expressions for the oscillation or rotational frequency, critical buckling force, and beating wavelength can be of general use for estimating motor forces in over-damped filament-motor systems. While the microscopic analogue of κ_a in such systems requires further study, our theoretical estimate for the transition to steady beating suggests the magnitude of noise (equilibrium or non-equilibrium) that will disrupt stable dynamics in these systems. Second, devices have recently been developed [32] in which fluid is pumped and mixed by externally actuated biomimetic cilia with sizes approaching those of biological cilia. At this scale, advection and diffusion compete to determine mass transport. While pumping and mixing regimes are currently spatially separated [32], using an array of polar chains and tuning noise (e.g. by changing temperature to modify κ_a) could drive transitions from periodic (pumping) to erratic (mixing) regimes.

Motivated by quasi-two-dimensional systems in which particle motions are over-damped and hydrodynamic interactions are screened, we have focused on the roles of elasticity, local activity, local friction and noise in governing filament dynamics. In future work, we will study how the dynamics might change in the presence of long-range hydrodynamic interactions. Relatedly, Jayaraman *et al.* [18] observed autonomous motions in a *noiseless* active filament

comprised force-free stresslet particles. Interestingly, in their model, the particles are not self-propelled in the manner that phoretic particles are, as individual particles are motionless when disconnected from the chain, and in contrast to our model they find that hydrodynamic interactions are essential for beating. The observation that self-generated periodic motions can arise from different fundamental driving forces suggests that they are a generic feature of internally active, slender filaments. In a broader context, in contrast to most studies of locomotion at low Reynolds number which prescribe the shape of the organism (typically as a slender

filament with prescribed kinematics), here we prescribe the active forces locally, and calculate the resulting shapes. If the anchored end does not have infinite resistance the self-propelled particles will propel the whole chain, the study of which is a natural next step.

Acknowledgement. Computational resources were provided by National Science Foundation through XSEDE computing resources and the Brandeis HPCC. We thank Howard Stone, Masaki Sano and Ronjo Adhikari for discussions during the preparation of this manuscript.

Funding statement. We acknowledge funding for this research provided by NSF-MRSEC-0820492 and the MacArthur Foundation (L.M.).

References

- Bray D. 2001 *Cell movements: from molecules to motility*. New York, NY: Garland Science.
- Fulford G, Blake J. 1986 Mucociliary transport in the lung. *J. Theor. Biol.* **121**, 381–402. (doi:10.1016/S0022-5193(86)80098-4)
- Nonaka S, Shiratori H, Saijoh Y, Hamada H. 2002 Determination of left–right patterning of the mouse embryo by artificial nodal flow. *Nature* **418**, 96–99. (doi:10.1038/nature00849)
- Sawamoto K *et al.* 2006 New neurons follow the flow of cerebrospinal fluid in the adult brain. *Science* **311**, 629–632. (doi:10.1126/science.1119133)
- Riedel-Kruse IH, Hilfinger A, Howard J, Jäijlicher F. 2007 How molecular motors shape the flagellar beat. *Hfsp J.* **1**, 192–208. (doi:10.2976/1.2773861)
- Sanchez T, Welch D, Nicastro D, Dogic Z. 2011 Cilia-like beating of active microtubule bundles. *Science* **333**, 456–459. (doi:10.1126/science.1203963)
- Dreyfus R, Baudry J, Roper M, Fermigier M, Stone H, Bibette J. 2005 Microscopic artificial swimmers. *Nature* **437**, 862–865. (doi:10.1038/nature04090)
- Masoud H, Bingham BI, Alexeev A. 2012 Designing maneuverable micro-swimmers actuated by responsive gel. *Soft Matter* **8**, 8944–8951. (doi:10.1039/C2SM25898F)
- Pooley CM, Balazs AC. 2007 Producing swimmers by coupling reaction–diffusion equations to a chemically responsive material. *Phys. Rev. E* **76**, 016308. (doi:10.1103/PhysRevE.76.016308)
- Palacci J, Cottin-Bizonne C, Ybert C, Bocquet L. 2010 Sedimentation and effective temperature of active colloidal suspensions. *Phys. Rev. Lett.* **105**, 088304. (doi:10.1103/PhysRevLett.105.088304)
- Paxton WF, Kistler KC, Olmeda CC, Sen A, St Angelo SK, Cao Y, Mallouk TE, Lammert PE, Crespi VH. 2004 Catalytic nanomotors: autonomous movement of striped nanorods. *J. Am. Chem. Soc.* **126**, 13 424–13 431. (doi:10.1021/ja047697z)
- Hong Y, Blackman NMK, Kopp ND, Sen A, Velegol D. 2007 Chemotaxis of nonbiological colloidal rods. *Phys. Rev. Lett.* **99**, 178103. (doi:10.1103/PhysRevLett.99.178103)
- Jiang H-R, Yoshinaga N, Sano M. 2010 Active motion of a Janus particle by self-thermophoresis in a defocused laser beam. *Phys. Rev. Lett.* **105**, 268302. (doi:10.1103/PhysRevLett.105.268302)
- Volpe G, Buttinoni I, Vogt D, Kummerer H-J, Bechinger C. 2011 Microswimmers in patterned environments. *Soft Matter* **7**, 8810–8815. (doi:10.1039/C1SM05960B)
- Narayan V, Ramaswamy S, Menon N. 2007 Long-lived giant number fluctuations in a swarming granular nematic. *Science* **317**, 105–108. (doi:10.1126/science.1140414)
- Kudrolli A, Lumay G, Volfson D, Tsimring LS. 2008 Swarming and swirling in self-propelled polar granular rods. *Phys. Rev. Lett.* **100**, 058001. (doi:10.1103/PhysRevLett.100.058001)
- Deseigne J, Dauchot O, Chaté H. 2010 Collective motion of vibrated polar disks. *Phys. Rev. Lett.* **105**, 098001. (doi:10.1103/PhysRevLett.105.098001)
- Jayaraman G, Ramachandran S, Ghose S, Laskar A, Bhamla MS, Kumar PBS, Adhikari R. 2012 Autonomous motility of active filaments due to spontaneous flow-symmetry breaking. *Phys. Rev. Lett.* **109**, 158302. (doi:10.1103/PhysRevLett.109.158302)
- Laskar A, Singh R, Ghose S, Jayaraman G, Kumar PBS, Adhikari R. 2013 Hydrodynamic instabilities provide a generic route to spontaneous biomimetic oscillations in chemomechanically active filaments. *Sci. Rep.* **3**, 1964. (doi:10.1038/srep01964)
- Euler L. 1982 Determinatio onerum, quae columnae gestare valent. In *Leonhardi Euleri Opera Omnia 2* (eds C Blanc, P de Haller), pp. 17–232.
- Keller J. 1960 The shape of the strongest column. *Arch. Ration. Mech. Anal.* **5**, 275–285. (doi:10.1007/BF00252909)
- Keller J, Niordson F. 1967 The tallest column. *J. Math. Mech.* **16**, 433–446. (doi:10.1512/iumj.1967.16.16029)
- Sekimoto K, Mori N, Tawda K, Toyoshima Y. 1995 Symmetry-breaking instabilities of an *in vitro* biological system. *Phys. Rev. Lett.* **75**, 172–175. (doi:10.1103/PhysRevLett.75.172)
- Woolley DM. 2007 A novel motility pattern in quail spermatozoa with implications for the mechanism of flagellar beating. *Biol. Cell.* **99**, 663–675. (doi:10.1042/BC20070050)
- Weeks JD, Chandler D, Andersen HC. 1971 Role of repulsive forces in determining equilibrium structure of simple liquids. *J. Chem. Phys.* **54**, 5237. (doi:10.1063/1.1674820)
- Gompper G, Ihle T, Kroll DM, Winkler RG. 2009 Multi-particle collision dynamics: a particle-based mesoscale simulation approach to the hydrodynamics of complex fluids. In *Advanced computer simulation approaches for soft matter sciences III* (eds C Holm, K Kremer), vol. 221 of *Advances in Polymer Science*, pp. 1–87. Berlin, Germany: Springer.
- Bourdieu L, Duke T, Elowitz M, Winkelmann D, Leibler S, Libchaber A. 1995 Spiral defects in motility assays: a measure of motor protein force. *Phys. Rev. Lett.* **75**, 176–179. (doi:10.1103/PhysRevLett.75.176)
- Hanggi P. 1986 Escape from a metastable state. *J. Stat. Phys.* **42**, 105–148. (doi:10.1007/BF01010843)
- Vutukuri HR, Demirors AF, Peng B, van Oostrum PDJ, Imhof A, van Blaaderen A. 2012 Colloidal analogues of charged and uncharged polymer chains with tunable stiffness. *Angew. Chem. Int. Ed.* **51**, 11 249–11 253. (doi:10.1002/anie.201202592)
- Sung KE, Vanapalli SA, Mukhija D, McKay HA, Millunchick JM, Burns MA, Solomon MJ. 2008 Programmable fluidic production of microparticles with configurable anisotropy. *J. Am. Chem. Soc.* **130**, 1335–1340. (doi:10.1021/ja0762700)
- Sacanna S, Irvine WTM, Chaikin PM, Pine DJ. 2010 Lock and key colloids. *Nature* **464**, 575–578. (doi:10.1038/nature08906)
- Shields AR, Fiser BL, Evans BA, Falvo MR, Washburn S, Superfine R. 2010 Biomimetic cilia arrays generate simultaneous pumping and mixing regimes. *Proc. Natl Acad. Sci. USA* **107**, 15 670–15 675. (doi:10.1073/pnas.1005127107)

Flagellar dynamics of a connected chain of active, Brownian particles

Electronic Supplementary Material

BY RAGHUNATH CHELAKKOT^{1,3}, ARVIND GOPINATH^{1,2}, L. MAHADEVAN^{3,4}, MICHAEL F. HAGAN¹

¹*Martin Fisher school of physics, Brandeis University, Waltham, MA 02453, USA*

²*Max Planck Institute for Dynamics and Self-Organization, Goettingen, Germany 037077*

³*School of Engineering and Applied Sciences, Harvard University, Cambridge, MA 02138, USA*

⁴*Department of Physics, Harvard University, Cambridge, MA 02138, USA*

Appendix A. Static solutions for a filament deformed by follower forces

In the continuum, noise-free limit one may coarse-grain the chain of connected active swimmers each of size σ and separated by b as a thin, elastic, inextensible filament of length ℓ provided $\kappa b^2/k_b T \gg 1$ and $\sigma/\ell \ll 1$. The filament bends due to the action of compressive, active forces and the constraint of inextensibility. Such an active filament, clamped vertically at one end and free at the other, remains stably vertical for small force (compression) densities. At a critical value of the force density however, the straight shape is unstable to lateral perturbations and yields to a buckled shape. Before buckling, the compressive forces all act vertically towards the clamped end and this scenario resembles the classical problem of a filament buckling under gravity. Originally proposed and solved by Euler (see the translated works of Euler [1]) this problem has been revisited again more recently [2, 3]. The correspondence arises due to the non-generic initial configuration with the filament clamped vertically.

To obtain an equation to test if static solutions can exist for our case, we first parametrize the shape of the column by the angle, $\theta(s, t)$, that the centerline makes with \mathbf{e}_x . We then decompose the force resultant at a point s along its length in terms of its cartesian components, $\mathbf{F} = F_x \mathbf{e}_x + F_y \mathbf{e}_y$. Torque and force balances on a elemental length yield (primes henceforth denoting differentiation with respect to arc-length, s) in the small deformation limit $\sin \theta \approx \theta$, $\kappa \theta''' = \theta'(F_x \cos \theta + F_y \sin \theta)$, $F'_x = f_p \cos \theta$ and $F'_y = f_p \sin \theta$. Since no external forces are present at the free end, we obtain

$$\theta''' + \beta(1 - s)\theta' = 0, \quad \beta \equiv \frac{f_p \ell^3}{\kappa} \quad (\text{A1})$$

where the constant $\beta \equiv (f_p \ell^3 / \kappa)$. This equation has a different form for a column buckling under its self weight. Specifically, for the latter case, the 2nd term on the left hand side has the form $((1 - s)\theta)'$ instead of $(1 - s)\theta'$. To check if steady small deformation solutions exist, we seek non-trivial solutions in terms of the Airy functions \mathcal{A} and \mathcal{B} . For boundary conditions $\theta(0) = 0$, $\theta'(1) = 0$ and $\theta''(1) = 0$, we set $\theta = \int_0^s Z(s') ds'$, and $\varphi \equiv \beta^{\frac{1}{3}}(s-1)$, to obtain $d^2/dZ^2 - \varphi Z = 0$, $Z(0) = 0$, $(dZ/d\varphi)(0) = 0$. Solutions of the form $Z = C_1 \mathcal{A}(\varphi) + C_2 \mathcal{B}(\varphi)$ satisfy the required boundary conditions provided $C_1 \mathcal{A}(0) + C_2 \mathcal{B}(0) = 0$, and $C_1 \mathcal{A}'(0) + C_2 \mathcal{B}'(0) = 0$ are satisfied simultaneously. This is possible only when $C_1 = 0$ and $C_2 = 0$. Our simulations suggest that the buckled large deformation solution is linearly unstable to either oscillating (flapping) instabilities or rotational instabilities depending on the boundary conditions.

Appendix B. Coarse grained continuum model for $\kappa_a^{-1} \rightarrow 0$

ESM Figure 1 is a schematic of the geometry and also shows the free-body diagram of the forces and torques acting on an elemental length of the filament. We coarse-grain the discrete filament of attached self-propelled Brownian particles into a continuous inextensible filament of length ℓ and diameter σ moving in the $x - y$ plane. The active compressive forces are also coarse-grained into a force density f_p acting anti-parallel to the tangent vector. Choosing the arc-length s as our variable, we locate the origin of our stationary co-ordinate system at the clamped base $s = 0$. The other end $s = \ell$ is free to move in the $x - y$ plane. The beating is characterized by the sequence of shapes generated as a test material point at s with Cartesian coordinates $(x_p(s), y_p(s))$ moves in the Newtonian liquid of viscosity μ . In the long aspect ratio limit $\ell/\sigma \gg 1$, the angle $\theta(s, t)$ made by the centerline of the inextensible filament with the x axis serves as a convenient indicator of the filament shape. With this parametrization, we can express the dual vectors tangent, $\mathbf{t}(s, t)$ and normal

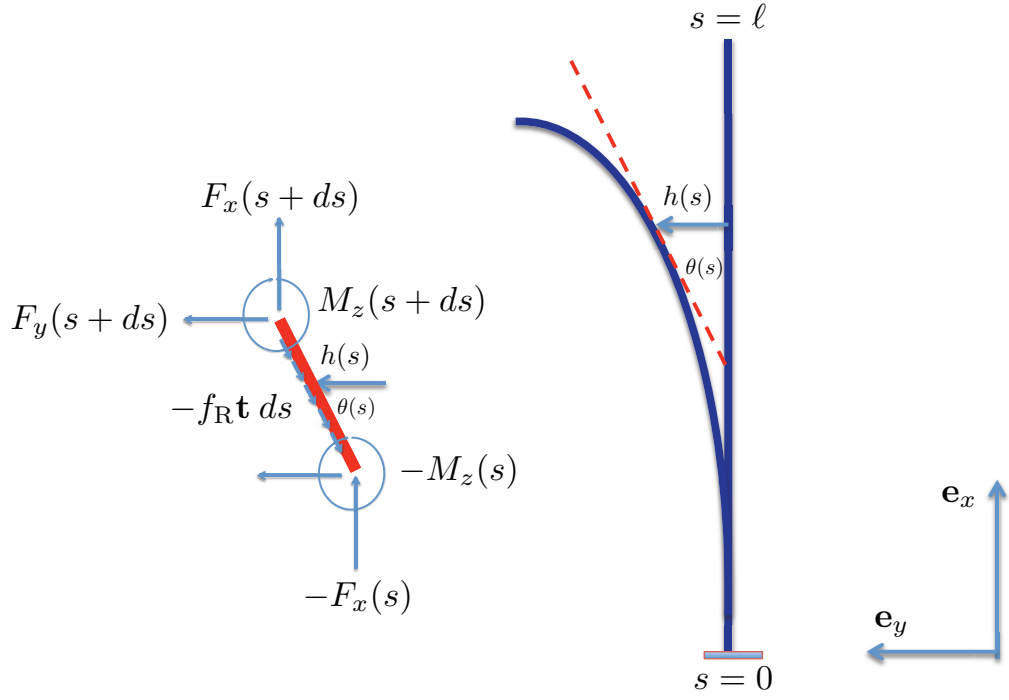


Figure 1. Schematic of the bent state and reference sketch showing the forces and torques acting on a elemental slice.

$\mathbf{n}(s, t)$ to the centerline solely in terms of $\theta(s, t)$. Note that at (x_p, y_p) , the increments along the Cartesian directions are related to ds by, $dx = \cos \theta ds$ and $dy = \sin \theta ds$.

We limit ourselves to small curvatures, $\sin \theta \approx \theta$, and thus only consider small forces that generate curvature radii that are much larger than σ . Referring to the free body diagram in ESM Fig. 1, we note that in the physically relevant non-inertial (small Reynolds number) limit, the viscous forces, elastic and active forces must balance. To make progress we decompose the total force resultant at a cross-section s , $\mathbf{F}(s, t)$ into its tangential T and normal N components

$$\mathbf{F} = T\mathbf{t} + N\mathbf{n}. \quad (\text{B } 1)$$

The passive forces per unit length consists of a viscous drag force per unit length and an artificial short-ranged repulsive force that prevents self-crossing implemented directly. The viscous force per unit length depends on the velocity field generated due to the motion of the filament segments.

For simplicity, we do not solve the full hydrodynamic problem, but instead use resistive-force theory for slender bodies - an approximation that is asymptotically valid for large aspect ratio filaments. Resistive-force theory can be formally deduced from slender-body theory by excluding the complete nonlocal relation between the deformation at one segment and the velocity field generated due to other moving segments but including only local drag. Ignoring non-locality leads to the local viscous force per unit length at s

$$\mathbf{f}_v(s) = -(\eta_{\parallel} u_{\parallel} \mathbf{t} + \eta_{\perp} u_{\perp} \mathbf{n}) \quad (\text{B } 2)$$

where η_{\parallel} is the effective viscous resistance per unit length for motion of the filament along the tangent, η_{\perp} is the resistance per unit length for motion along the local normal, u_{\parallel} is local velocity of the centerline along the tangent vector and u_{\perp} is the filament velocity along the normal. The friction coefficients are

$$\eta_{\perp} = 4\mu\pi \left(\ln \frac{\ell}{2a} + \frac{1}{2} \right)^{-1}, \quad \text{and} \quad \eta_{\parallel} = 2\mu\pi \left(\ln \frac{\ell}{2a} + \frac{1}{2} \right)^{-1}$$

where μ is the viscosity of the ambient fluid, ℓ the total contour length of the filament, and a the filament radius. Note that we have kept only the leading order terms in the logarithm of the initial aspect ratio. The assumptions leading to (B-1) lead to some minor qualitative and quantitative differences with the exact theory (see section C). However these limitations do not prevent the approximate theory from capturing the essential physics of the phenomena we wish to study, such as the onset of buckling instabilities, the subsequent evolution of complex shapes, and our scaling predictions for the final stable dynamical behaviour.

With the resistive-force approximation for the viscous drag, the overall force balance becomes

$$-\mathbf{F}(s) + \mathbf{F}(s + ds) - f_p \mathbf{t} ds = -\mathbf{f}_v. \quad (\text{B } 3)$$

Using $\mathbf{F}' = (T' - N\theta')\mathbf{t} + (N' + T\theta')\mathbf{n}$ we balance force components to obtain the equations $(N' + T\theta') = \eta_{\perp}u_{\perp}$ and $(T' - N\theta') = \eta_{\parallel}u_{\parallel} + f_p$. A balance of moments acting on the differential element yields

$$\mathbf{M}' + \mathbf{t} \times (N\mathbf{n} + T\mathbf{t}) = 0 \quad (\text{B } 4)$$

Combining all the above expressions, we can eliminate N and relate the bending moment per unit length to the angle θ using $M = \kappa\theta'$ to finally obtain the coupled non-linear equations for the tension, T and angle θ

$$-\kappa\theta''' + T\theta' = \eta_{\perp}u_{\perp} \quad (\text{B } 5)$$

$$T' + \kappa\theta''\theta' - f_p = \eta_{\parallel}u_{\parallel} \quad (\text{B } 6)$$

To close these equations, we need to relate the velocity of the filament to its shape and properties. For an inextensible filament $\frac{ds}{dt} = 0$, $\frac{d\mathbf{t}}{dt} = \frac{d\theta}{dt}\mathbf{n} = \frac{\partial\theta}{\partial t}\mathbf{n}$ so that $\frac{d\mathbf{t}}{dt} = (u'_{\parallel} - \theta'u_{\perp})\mathbf{t} + (u'_{\perp} + \theta'u_{\parallel})\mathbf{n}$ [4, 5]. Using these expressions to eliminate the filament velocities in favor of the filament shape and shape changes and indicating derivatives with respect to time as subscripts, we find $\theta_t = u'_{\perp} + u_{\parallel}\theta'$ and $u'_{\parallel} - u_{\perp}\theta' = 0$ and consequently

$$T'' = -\kappa(\theta''\theta')' + (f_p)' + \frac{\eta_{\parallel}}{\eta_{\perp}}\theta'(-\kappa\theta''' + T\theta') \quad (\text{B } 7)$$

and

$$\eta_{\perp}\theta_t = -\kappa\theta'''' + (T\theta')' + \frac{\eta_{\perp}}{\eta_{\parallel}}\theta'(T' + \kappa\theta''\theta' - f_p). \quad (\text{B } 8)$$

A full numerical solution to these equations under the constraint $\eta_{\perp} = \eta_{\parallel}$ will yield the pre-factors to the mean-field scalings described in the text.

Let us first seek steady solutions or base states to these equations. We specify the initial shape to be a constant angle $\theta = \theta_0$ and tension $T = T_0(s)$ where the arc-length s is measured from the fixed end (head). Expanding to linear order in a small and as yet unknown amplitude, on using $T = T_0(s) + \epsilon T_1(s, t)$ and $\theta = \theta_0 + \epsilon\theta_1(s, t)$, we obtain

$$\begin{aligned} T_0'' &= f_p', \\ \eta_{\perp}(\theta_1)_t &= -\kappa(\theta_1)'''' + (T_0\theta_1')' + \frac{\eta_{\perp}}{\eta_{\parallel}}\theta_1'(T_0' - f_p). \end{aligned} \quad (\text{B } 9)$$

Since there is no tension without f_p , we require $T_0(s) = 0$ when $f_p = 0$. Additionally there is no tension at $s = \ell$ and thus $T_0(s) = (s - \ell)f_p$. The lone equation for the the angle results in

$$\eta_{\perp}(\theta_1)_t = -\kappa(\theta_1)'''' + ((s - \ell)f_p\theta_1')' \quad (\text{B } 10)$$

and thus interestingly the ratio of viscosities drops out to linear order and small deformations; however, this is true only at onset. We then keep the bending term to $O(1)$ and drop the subscript 1 to obtain the dimensionless form

$$\gamma\theta_t + \theta'''' + (\beta(1 - s)\theta')' = 0 \quad (\text{B } 11)$$

where $\gamma \equiv (\eta_{\perp}\omega\ell^4/\kappa)$ is a dimensionless frequency and the parameter $\beta \equiv f_p\ell^3/\kappa$ is the same parameter as in ESM Eq. A 1.

For small deformations, one can simplify the equation further using the Monge approximation. Setting $\theta \approx Z'$ where Z is a scaled transverse deflection from the base state, we get upon integrating once with respect to arc-length

$$\gamma Z_t + Z'''' + \beta(1 - s)Z'' = a(t) \quad (\text{B } 12)$$

In the absence of viscosity $\gamma \rightarrow 0^+$, $a(t) = 0$ and thus we set it to zero. Redefining $\eta = (1 - s)$

$$\gamma Z_t = -Z_{\eta\eta\eta\eta} - \beta(\eta Z_{\eta\eta}), \quad (\text{B } 13)$$

with $Z(1) = 0$, $Z'(1) = 0$, $Z''(0) = 0$ and $Z'''(0) = 0$ for the clamped head and $Z(1) = 0$, $Z''(1) = 0$, $Z'(0) = 0$ and $Z'''(0) = 0$ for the pivoted head. This equation matches the equations analysed by Sekimoto *et. al.* [6] and confirms that the simplified forms are valid only at onset and for small deformations and for weak curvatures - i.e., small lengths and small active forces. These predictions are confirmed by our full non-linear far from critical solutions.

We note however that the scaling for the frequency obtained by Sekimoto *et. al.* corresponds only to short relatively stiff filaments and does not give the right dependence on the active force density, f_p . The correct scaling valid away from onset is obtained by recognising that the right length scale is not the filament length ℓ but the characteristic wavelength λ of the deformed shapes (see Eq. 3.2 of the main text).

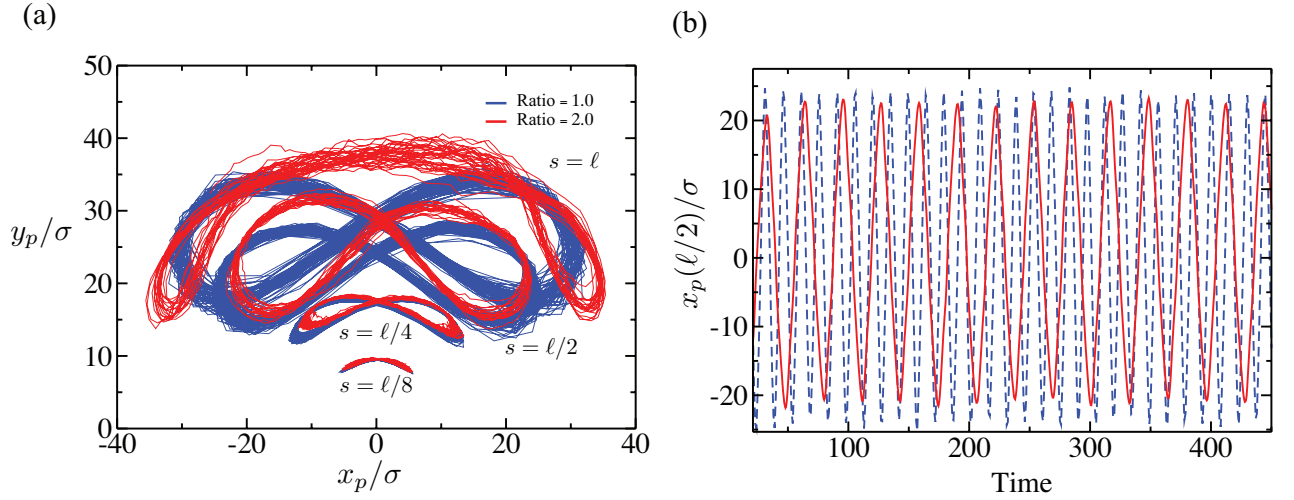


Figure 2. (a) Trajectories of material points on the filament with a clamped boundary condition, with $\eta_{\perp}/\eta_{\parallel} = 1$ (blue) and $\eta_{\perp}/\eta_{\parallel} = 2$ (red). (b) The lateral position of a material point of the clamped filament as a function of time with $\eta_{\perp}/\eta_{\parallel} = 1$ (blue) and $\eta_{\perp}/\eta_{\parallel} = 2$ (red). The filament length is $\ell = 80$, the active force density is $f_p = 20$, and with weak angular noise $\kappa_a = 20$. As expected increasing the normal resistivity reduces the frequency in accordance with the scaling expectation.

Appendix C. The effects of anisotropic viscous friction and long-range hydrodynamic interactions

The coupled fluid flow and filament deformation, including non-local coupling (due to fluid incompressibility), comprises a complicated highly non-linear problem. As mentioned in appendix B, to this point we have not solved the full hydrodynamic problem, but instead we have used resistive-force theory for slender bodies. We are motivated to do this by the nature of the experimental systems that motivate our model. For example, in an over-damped quasi-2D system, the effects of confinement rapidly cut off long-range hydrodynamic interactions (HI). Furthermore, motor-filament assays involve elastic filaments moving in highly damping medium and thus a local approximation is not physically unrealistic. Finally, in the case of a granular shake table system, there will be no long-range HI. In this appendix we use simulations to evaluate the effect of two approximations related to HI.

Anisotropic mobility. As noted above, the simulations in the main text consider anisotropic filament mobility ($\eta_{\perp}/\eta_{\parallel} = 1$), which corresponds to the Rouse model for an active chain with freely draining hydrodynamics, and would be an appropriate description for a chain in a granular shake table system where there is no HI. To characterize the effect of anisotropic mobility, beating waveforms and frequencies are compared between filaments with isotropic mobility and those with ($\eta_{\perp}/\eta_{\parallel} = 2$), corresponding to the ideal slender body limit of a large aspect ratio rod in a Newtonian solvent. We observe that changing the mobility ratio while keeping η_{\parallel} fixed, leads to quantitative differences – the beating frequency approximately halves (smaller frequency for larger normal resistivity η_{\perp}) due to the increase in η_{\perp} (see Eq. 3.3 in the main text) and the trajectory narrows since longitudinal motions are preferred over transverse motions. However, the trajectory shapes are qualitatively the same, and the scaling laws for critical propulsion force and frequency are still satisfied. Furthermore, the effect of noise is the same as before (see ESM Figure 2).

Long-range HI. We performed an additional set of simulations incorporating non-local hydrodynamic interactions (HI) in the limit $\kappa_a \rightarrow \infty$. We used a hybrid simulation technique, in which molecular dynamics simulations for the filament were combined with a mesoscale hydrodynamic simulation method called multi-particle collision dynamics (MPC) for solvent [7]. In this approach we model the solvent as a collection of N point-like particles of mass m , whose velocities are determined by a stochastic process. Two steps are performed at each time point to evolve a trajectory. In the streaming step, the particles move ballistically for a time interval h that may be understood as a mean collision time. In the second step (the collision step), the particles are sorted to cells of a square lattice with lattice constant a , and the particle velocities, relative to the center-of-mass velocities of the cell, are rotated by an angle α . The direction of rotation is chosen randomly. The dynamics of the active filament is meanwhile simulated using a standard velocity-Verlet algorithm, and the filament-fluid interaction is implemented by including the filament monomers in the collision step and allowing for the appropriate momentum transfer. Simulation parameters for the solvent were $\alpha = 130^\circ$, $h = \sqrt{ma^2/k_B T}$, and the mean number of particles per cell $\langle N \rangle = 20$. For the filament, the

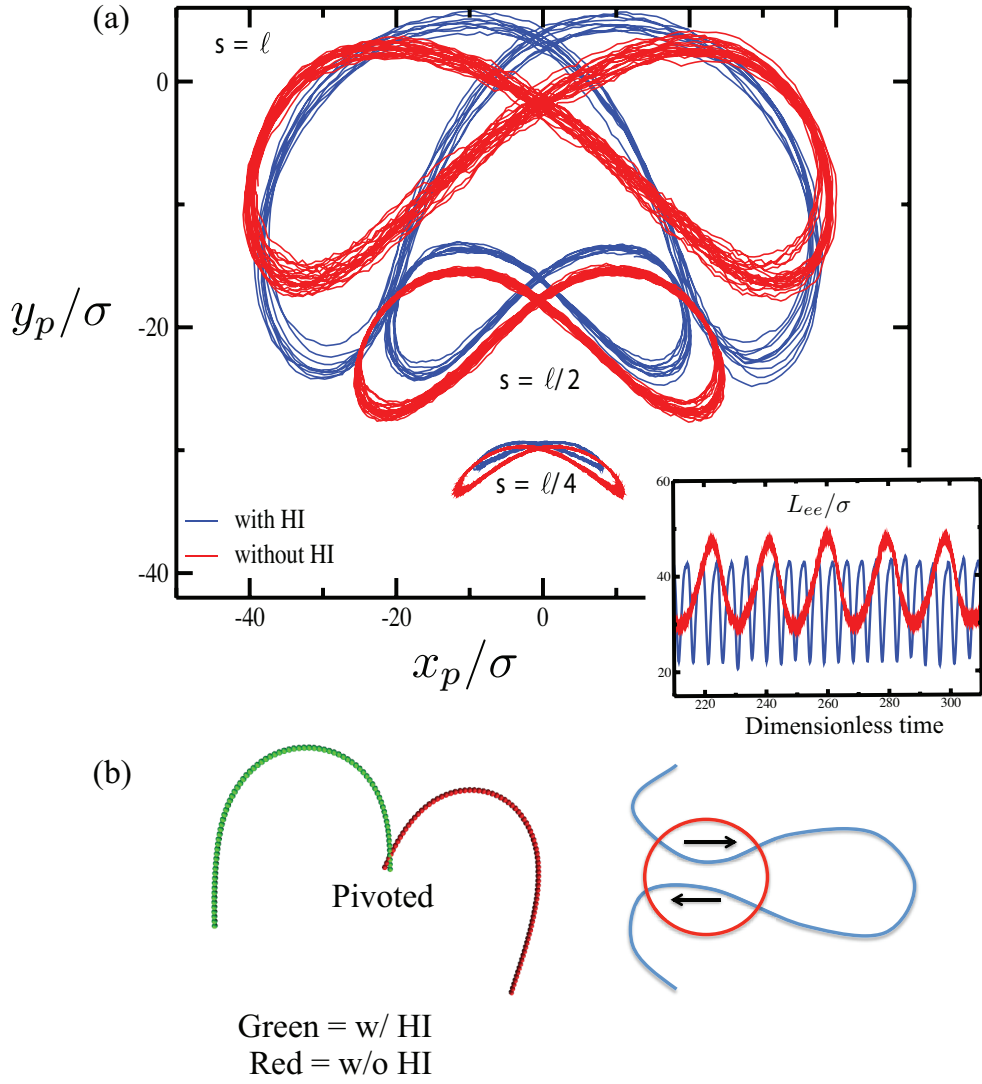


Figure 3. (a) Trajectories of material points on the filament with a clamped boundary condition, with (blue) and without (red) non-local hydrodynamic interactions (HI). Inset: the end-to-end distance L_{ee} of beating filaments as a function of time. (b) The configurations of a filament with a pivoting boundary condition for simulations with (green) and without (red) non-local HI. For (a) and (b) the filament length is $\ell = 80$, the active force density is $f_p = 10$, and weak angular noise $\kappa_a = 20$. (c) Schematic of a filament configuration where relative motions of adjacent filaments encounter increased viscous drag when non-local HI are considered.

monomer mass $M = m\langle N \rangle$, the bond length was $b = a$, and the monomer diameter was $\sigma = b$. A constant temperature was maintained by local rescaling of the solvent velocity.

The dynamical behaviors of both clamped and pivoting filaments with and without non-local HI are compared in ESM Figure 3. For the clamped boundary condition, we found the same critical active force density for buckling f_c as for the simplified local hydrodynamics model, and for $f_p > f_c$ the filament interacting via non-local HI displays the same flagella-like beating as does the simplified model. Furthermore the expression for beating frequency as a function of active force density f_p is the same in both cases. Inclusion of non-local HI gives rise to an effectively anisotropic mobility yielding a difference in the frequency in comparison to the local HI, isotropic mobility result - as seen in Figure 3(a). However the scaling of the frequency in terms of the dependence on viscosity, κ and f_p remains unchanged. A detailed comparison of the beating patterns of the two predictions is made by tracking specific material points along the filament contour. We plot in the trajectories of the three material points located at $s = \ell/4$, $\ell/2$ and ℓ when $\ell = 80$. The results demonstrate that beating patterns in the presence and absence of non-local HI are qualitatively similar, with the model filament transcribing a figure-of-eight in both cases.

We see that including non-local HI for the driven polar filament leads to slightly smaller lateral amplitudes and increases the beating frequency. The reduction in both relative motions between filament parts as well

as a reduction in beating amplitude (due to the increased viscous interactions) when combined with the constant energy input due to activity may account for the increase in frequency. However, we reiterate that the differences in beating patterns with and without HI are not qualitative and that expressions for the frequency in terms of the active force density, f_p and the critical force for buckling are the same. In addition, for the pivoted an boundary condition, simulations with non-local HI yield rotating filaments with similar shapes as found for the local HI model.

Note that in our simulations the filament is constrained from global translation due to the clamped or pivoted and boundary condition. This attachment point can support any force or torque needed to maintain the clamped end. Thus our simulations over-emphasize hydrodynamic interactions when compared to a chain of truly force-free particles. A systematic analysis of the changes in beating frequencies and shapes of long, self interacting filaments, due to fluid mediated interactions is a topic for our future study.

The fact that including long-range HI in our simulations does not qualitatively change the behavior can be understood by considering the effective long-range HI in typical filament trajectories. For example, in the long-filament limit of the clamped boundary condition case, the filaments form highly meandering loops that slide past each other in close proximity. Nonlocal intra-filament viscous interactions are indeed important in this case, but the extra viscous friction in a 2D system for relative sliding motions has a logarithmic dependence on the gap between the segments and for very small gaps (eventually) these interactions are subdominant compared to the excluded volume constraint. In the long-filament limit of the pivoted boundary condition case, the filaments form tightly coiled loops that rotate as a single unit. At long times there is no relative motion between adjacent coils (as long as there is excluded volume) and hence HI do not play a major role.

Appendix D. A first passage time calculation for finite κ_a

We now focus on the boundary between erratic and regular beating. Since the exact dynamics of the polar spheres is complicated, we adopt a simplified picture that combines certain coarse-grained continuum aspects with first passage time calculations based on the role of noise in disrupting aligned configurations.

Our initial condition is a vertical filament - this special orientation results in a critical load for buckling before erratic or sustained oscillations can occur. It is easiest to imagine coarse-graining the active force, $f_p(s)$ at every point along the filament into an average part (averaged over many microscopic rotary diffusion time scales) and a rapidly fluctuating part: $f_p(s) = \overline{f_p}(s) + \hat{f}_p(s)$. These fluctuations arise due to thermal noise and manifest in the local orientation field escaping from a favorable configuration (anti-parallel to the tangent) to an unfavorable configuration where the active force contribution is negligible - chosen to be along the normal, $\mathbf{n}(s)$. The relative magnitudes of these two components control the dynamical response. Thus in the noise-dominated limit, the averaged component is negligible while in the noiseless limit there are no fluctuations.

In the diffusion (noise) dominated limit $\kappa_a \ll 1$, the active, polar spheres are very animated, re-orienting themselves constantly with respect to their neighbors and over very small time scales. The filament does not undergo correlated beating in this limit - rather we can either have irregular beating when $\overline{f_p}(s)$ is greater than the force density required for buckling or no beating at all. In fact for very small values of κ_a , we do not expect any beating due to noise. For $\kappa_a \gg 1$, simulations demonstrate three distinct regimes. For low propulsion forces below the critical value $f_p < f_c$, we do not observe any statistically significant beating - the straight configuration remains stable and variations in $\langle L_{ee} \rangle \simeq \ell$ due to fluctuations in the directions of \mathbf{p}_i are insignificant. As f_p increases with κ_a held constant, we go from the no-beating regime (A) to an intermediate irregular beating regime (B) and finally to the regular beating regime (C). The critical active force density curves that separate the transitions A \rightarrow B and B \rightarrow C depend on the passive filament elasticity through the values of ℓ and κ and on the amplitude of the noise in propulsion correlations through κ_a .

Consider first the continuum noise-free results. As the amplitude of the noise (in our case κ_a^{-1}) tends to zero, the effective time for the polarity field to flip from the compressive to extensional configuration (or in other words to escape from the compressive configuration) diverges due to the high energetic barrier to rotation of polarity vectors. Thus for $f_p < f_c$, the filament is straight and for $f_p > f_c$ the filament first buckles and then oscillates with frequency that scales as $f_p^{4/3}$.

With this in mind, consider fixing the active density f_p to a value greater than f_c and then subsequently varying κ_a to identify the role of noise in the system. As alluded to in the main text, with increasing κ_a *there is increasing correlation between the sphere self-propulsion directions as well as an increasing time over which the correlations are sustained*. In the noise-less limit, the polarity vector $\hat{\mathbf{p}}(s)$ (direction of self-propulsion) tends to point along the filament (anti-parallel to the tangent directed along increasing s). Noise introduces a characteristic time, T_c , for which the propulsion direction acts to compress the filament. We hypothesize

that irregular beating (regime B) arises whenever the correlation time is shorter than the filament oscillatory timescale in the noiseless, perfectly aligned limit, i.e. $T_f \sim \eta_\perp (\kappa/f_p^4)^{1/3}$. In summary, irregular beating arises when $T_c \ll T_B$ while regular beating (regime C) arises when $T_B \gg T_c$. Thus we expect the critical curve characterizing the B \rightarrow C transition to satisfy $T_f \sim T_c$.

The final part of the analysis requires estimating this correlation time T_c . While a complete calculation of this is complicated, an asymptotically accurate estimate can be obtained in the over-damped, viscosity controlled limit gives. The review by Hanggi [8] and the references therein provide a detailed description of how this simplification may be achieved. For now, we obtain a simple analytical result based on the theory for moderate to large friction elucidated therein.

We start from the assumption that the time scales of the dynamics of the polar particles (each with mass m) and motions of the heat bath held at temperature T are disparate. In the Markovian limit, the generalized Brownian dynamics governing the evolution of the polarity field with the noise being approximated by Gaussian white noise is

$$\zeta_{tt} = -\frac{1}{m} \frac{\partial U}{\partial \zeta} - \gamma_b \zeta_t + \eta(t) \quad (D 1)$$

with

$$\langle \eta(t) \eta(t') \rangle = \left(\frac{2k_B T \gamma_b}{m} \right) \delta(t - t'). \quad (D 2)$$

Now we rewrite the harmonic angular potential, $U_a = \frac{\kappa_a}{2} (\hat{\mathbf{p}} - \mathbf{b})^2$ in terms of an appropriate angle ζ , $U_a = \kappa_a (1 - \cos \zeta)$. We note that the potential is periodic - not a double well potential - and is characterised by regularly spaced troughs and valleys. The parameter T_c corresponds to a typical mean passage time for a critical number of self-propulsion directions within a local patch of spheres to escape from a perfectly aligned configuration, in which they drive filament compression, to a stable non-compressive configuration. For the calculation we choose the latter to be a configuration in which the polarity vector and the local tangent are in the same direction ($\zeta = \pi$) so that the forces are extensional and thus no compressive instabilities are possible. The energy difference between the two configurations $\zeta = 0$ and $\zeta = \pi$ respectively is in dimensionless units $2\kappa_a$. For $\kappa_a > 1$, equilibration in ζ may be assumed, with the polar spheres crossing the barrier diffusively. In the over-damped limit, this flux can be related to a frequency of crossover or the disrupting frequency.

Assuming a uniform relaxation rate $m\gamma_b$ we note that the polarity evolves in a 2π periodic domain with $\zeta = 0$ and $\zeta = 2\pi$ being the same orientation. The pseudo barrier - corresponding to when the polarity field acts so as to extend the filament is at $\zeta = \pi$. Following Hanggi's arguments, we note that the Langevin dynamics may be recast in the form of a Klein-Kramers equation. Since our simulations are in the over-damped friction dominated limit, we may assume for simplicity that thermal equilibrium in the well is maintained at all times and vertical thermalization occurs fast enough that deviations from the Boltzmann probability are negligible. It has been shown earlier that in this regime, the rate of escape is limited by a collision-dominated flux near the top of the pseudo-barrier. Hanggi evaluates the escape flux in this limit to obtain the classical Kramer's expression for the thermally activated escape rate $\Gamma \sim \left[\left(\frac{\gamma_b^2}{4} + \omega_b^2 \right)^{\frac{1}{2}} - \frac{\gamma_b}{2} \right] \left(\frac{\omega_0}{\omega_b 2\pi} \right) e^{-2\kappa_a}$. Here γ_b depends on the resistivity in the vicinity of the escape point ($\zeta = \pi$), the frequency at the base of the well is given by $\omega_0 \sim |U_a''(0)|^{\frac{1}{2}} \sim \sqrt{\kappa_a}$ and the frequency at the top of the hill is given by $\omega_b \sim |U_a''(\pi)|^{\frac{1}{2}} \sim \sqrt{\kappa_a}$. The friction-induced transmission frequency μ in the over damped limit satisfies $\mu \approx \left[\frac{\gamma_b}{2} \left(1 + 2 \frac{\omega_b^2}{\gamma_b^2} \right) - \frac{\gamma_b}{2} \right] \approx \left(\frac{\omega_b^2}{\gamma_b} \right)$ using which we obtain the asymptotically correct result for the escape frequency, $\Gamma \sim \left(\frac{\omega_0 \omega_b}{2\pi \gamma_b} \right) e^{-2\kappa_a}$. Since the diffusivity and thus the viscosity are constant in all our simulations, we ignore multiplicative factors. Setting this frequency to be of the same order as the zero-noise frequency we obtain a preliminary estimate for the critical line of $f_p \sim \kappa_a^{3/4} (e^{-2\kappa_a})^{3/4}$. This estimate needs to be modified as follows. First, a non-zero critical density for buckling arises due to the non-generic initial configuration. However far from criticality, the net force determines the beat frequency. Thus we introduce A , a parameter obtained from the critical force in the noise-less limit (and hence not an adjustable parameter) that ensures that the critical force tends to the noiseless continuum limit as $\kappa_a \rightarrow \infty$. Second, the irregular beating behavior requires that a critical number of motors escape from the well, which we account for by introducing a pre-factor. Satisfying these conditions leads to the dimensionless form

$$f_p \sim \frac{\kappa}{\ell^3} \left(A + B \kappa_a^{\frac{3}{4}} (e^{-2\kappa_a})^{\frac{3}{4}} \right). \quad (D 3)$$

References

- [1] Euler, L. 1982 Determinatio onerum, quae columnae gestare valent. *Leonhardi Euleri Opera Omnia 2 C. Blanc and P. de Haller, eds.*, **17**(), 232. doi:.

- [2] Keller, J. 1960 The shape of the strongest column. *Arch. Rational Mech. Anal*, **5**(1), 275–285. doi:10.1007/BF00252909.
- [3] Keller, J. & Niordson, F. 1967 The tallest column. *J. Math. Mech*, **16**(5), 433–446. doi:10.1512/iumj.1967.16.16029.
- [4] Happel, J. & Brenner, H. 1983 *Low Reynolds number hydrodynamics: with special applications to particulate media. Vol. 1*. Springer.
- [5] Roper, M., Dreyfis, R., Baudry, J., Fermigier, M., Bibette, J. & Stone, H. A. 2006 On the dynamics of magnetically driven elastic filaments. *Journal of Fluid Mechanics*, **554**, 167–190. doi:10.1017/S0022112006009049.
- [6] Sekimoto, K., Mori, N., Tawda, K. & Toyoshima, Y. 1995 Symmetry -breaking instabilities of an in-vitro biological system. *Phys. Rev. Lett.*, **75**(1), 172–175. doi:10.1103/PhysRevLett.75.172.
- [7] Gompper, G., Ihle, T., Kroll, D. M. & Winkler, R. G. 2009 Multi-Particle Collision Dynamics: A Particle-Based Mesoscale Simulation Approach to the Hydrodynamics of Complex Fluids. In *ADVANCED COMPUTER SIMULATION APPROACHES FOR SOFT MATTER SCIENCES III* (ed. Holm, C and Kremer, K), vol. 221 of *Advances in Polymer Science*, pp. 1–87. doi:10.1007/12.2008.5.
- [8] Hanggi, P. 1986 Escape from a metastable state. *J. Stat. Phys.*, **42**(1-2), 105–148. doi:10.1007/BF01010843.